Supplementary Information

Superlubricity under ultrahigh contact pressure enabled by partially oxidized black phosphorus nanosheets

Xiaoyong Ren[1†], Xiao Yang[1†], Guoxin Xie[1*], Feng He[1], Rong Wang[1], Chenhui Zhang[1], Dan Guo[1], Jianbin Luo[1*]

[1] *State Key Laboratory of Tribology, Department of Mechanical Engineering, Tsinghua University, Beijing 100084, China*

[†] *These authors contributed equally to this work*

[*] *Corresponding author, E-mail: xgx2014@tsinghua.edu.cn; luojb@tsinghua.edu.cn*

1. Supplementary Figures

The BP powders were prepared through the high-energy ball-milling method by using the red phosphorus (RP, purity > 99%, Aladdin Ltd.) as the raw material. In brief, 2 g RP powder was added into the steel jar (50 mL), and then it was sealed after filling with argon gas. The powder was ball milled for 20 h at a speed of 800 rpm with the steel balls as the ball-milling medium, and the ball-to-powder weight ratio was 50:1. **Supplementary Figure 1** shows the characterization of the initial RP and prepared BP powders. It can be seen that the shape of the BP particles is irregular, and the size ranges from several to tens of micrometer. The EDX spectrum shows that the dominant component is phosphorus with a small quantity of oxygen. After the long-time ball mill, the diffraction peaks of RP disappear, and instead distinct diffraction peaks appear at 2θ=16.9, 26.7, 35 and 50.8°, being consistent with the (020), (021), (040) and (060) planes of the standard orthorhombic BP (JCPDS No. 76-1957). The Raman spectra analysis also confirms the successful preparation of BP. Peaks at 361, 438 and 466 cm^{-1} are assigned to the A_g^1, B_{2g} and A_g^2 phonon modes for the bulk BP. These characterizations confirm the successful preparation of BP powders by the high energy ball-milling technique.

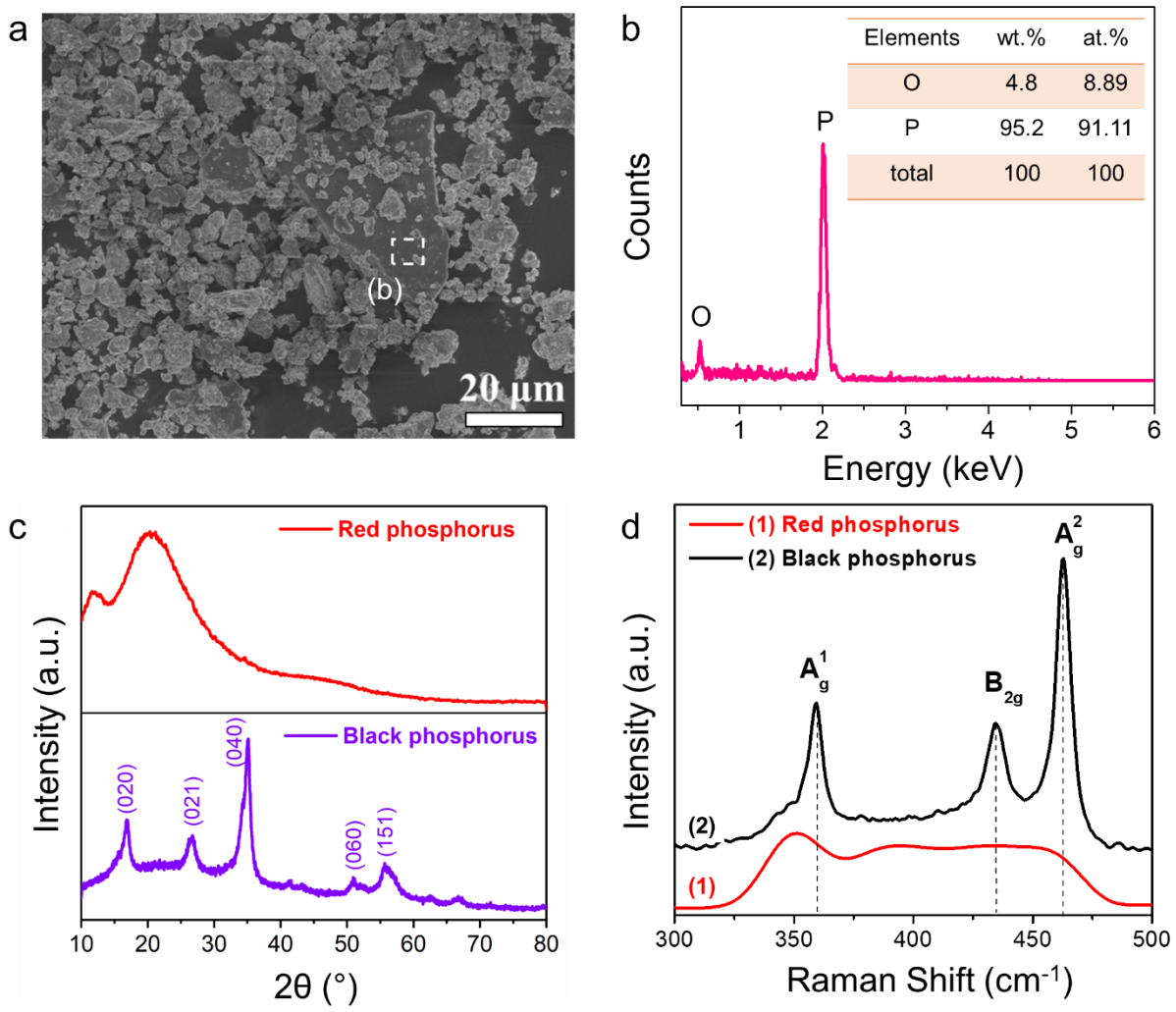

Supplementary Figure 1. Characterization of the RP and the prepared BP powders: **(a)** typical SEM image and **(b)** the EDX spectrum in figure (a); **(c)** XRD patterns and **(d)** Raman spectra of the initial RP and prepared BP powders.

Supplementary Figure 2 shows the macroscopic color changes with time of the BP aqueous suspension after adding different contents of HP, indicating the oxidation level of the BP nanosheets. It can be seen that the higher the ratio between H_2O_2 (μL) and BP (mg), the faster is the degraded speed of oBP. When the ratio is higher than 7.5, the solution even becomes transparent after 2 h, because of the degradation of the oBP nanosheets. The color of the oBP nanosheets aqueous suspension with a ratio of 1.5 between H_2O_2 (μL) and BP (mg) keeps deep black even after 20 h oxidization. The oBP nanosheets aqueous suspension with the ratio of 1.5 between H_2O_2 (μL) and BP (mg) can keep stable for days if it is kept without oxygen and light.

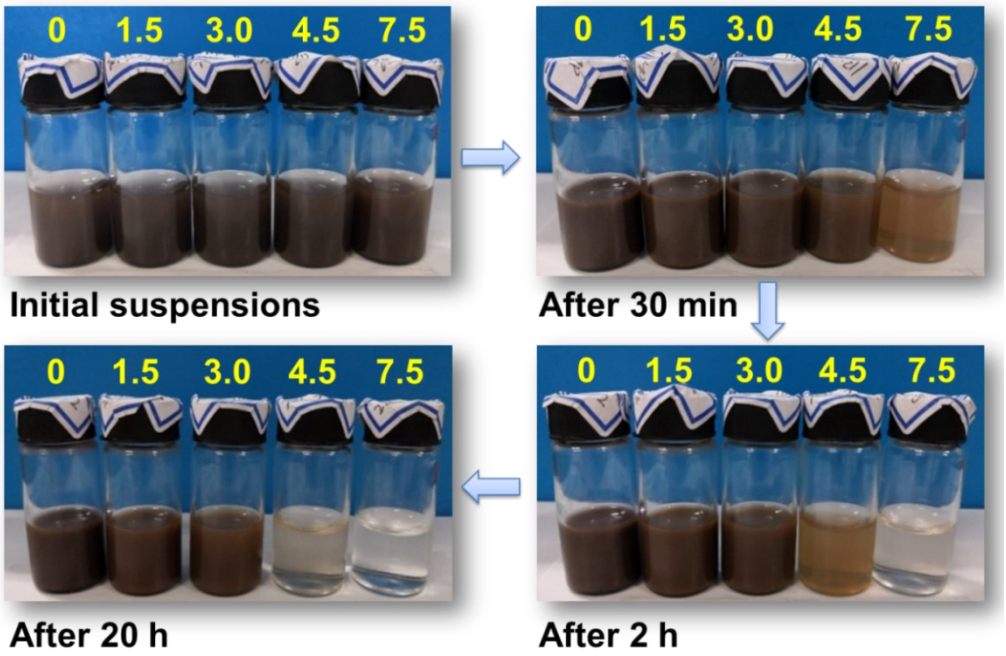

Supplementary Figure 2. Color changes with time of the BP aqueous suspensions after adding different contents of H_2O_2, indicating the oxidized extent of the BP. The yellow numbers above the bottle mean the ratio between H_2O_2 (μL) and BP (mg).

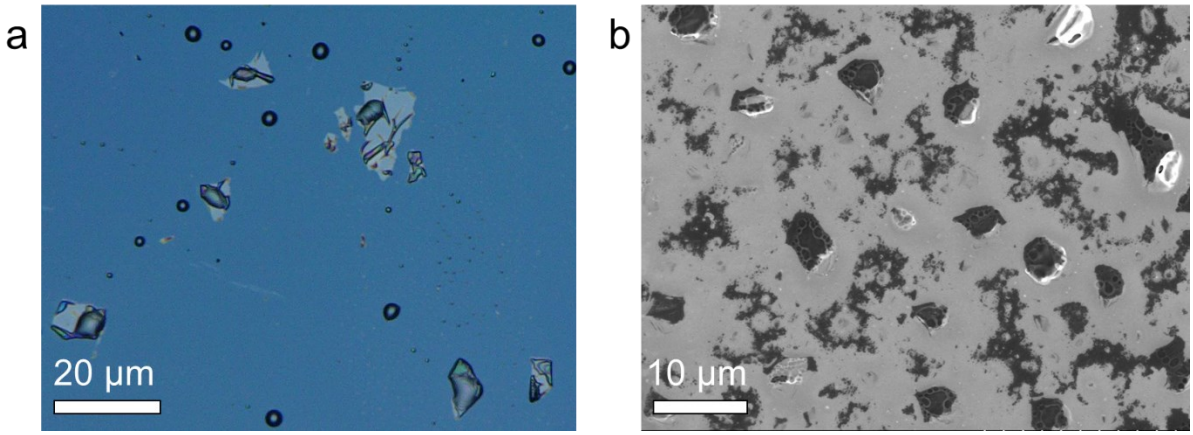

Supplementary Figure 3. (a) Optical and **(b)** SEM images of the obtained oBP nanosheets.

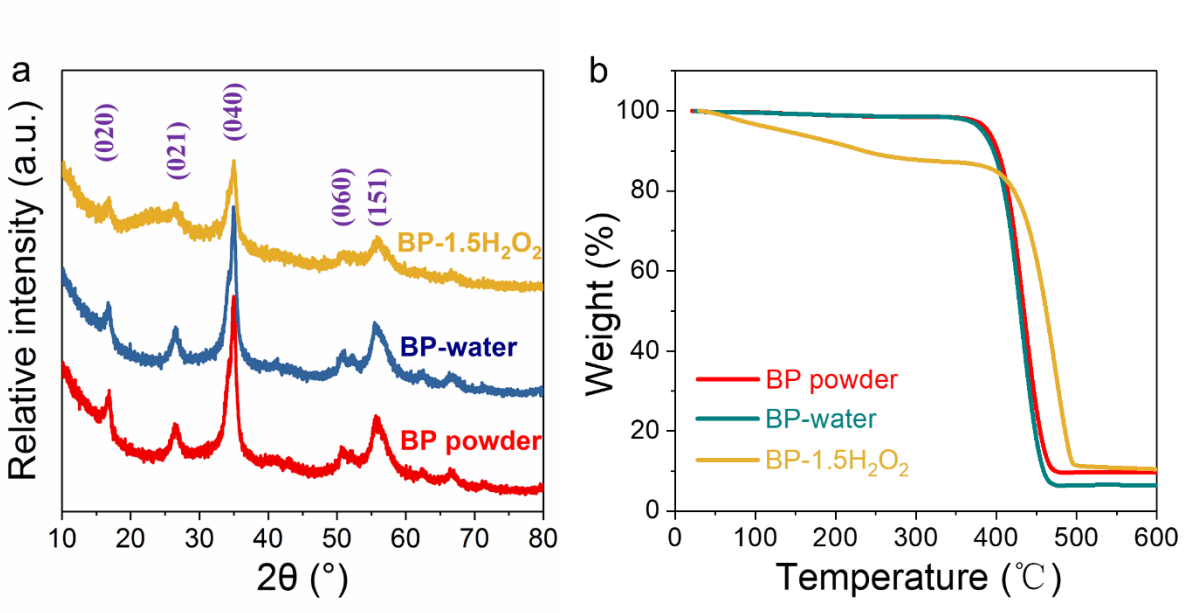

Supplementary Figure 4. (a) XRD patterns and **(b)** TGA of the initial BP, BP-water and BP-1.5H_2O_2 powders.

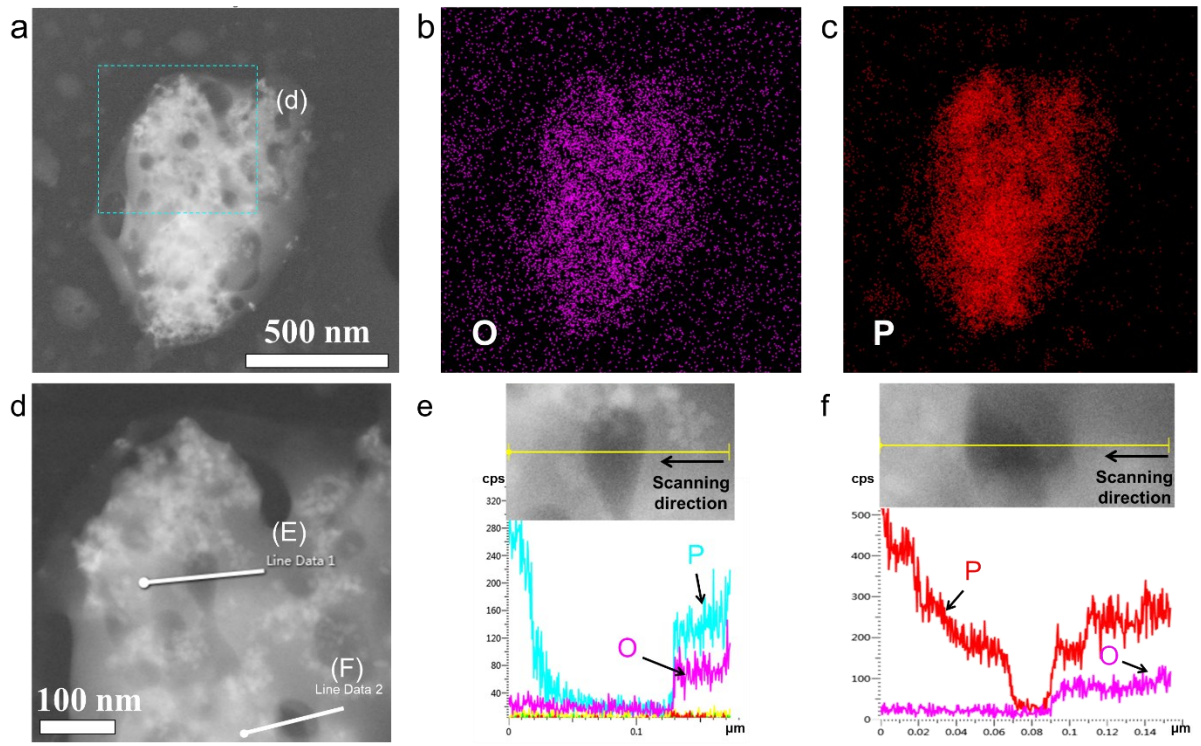

Supplementary Figure 5. (a) TEM image of the oBP nanosheet and the EDS mapping of **(b)** O and **(c)** P elements. **(d)** larger view of the zone in (a) and the corresponding line scanning spectra **(e)** and **(f)** on the porous structure, indicating the distributions of elements and the instability of structures under electron irradiation.

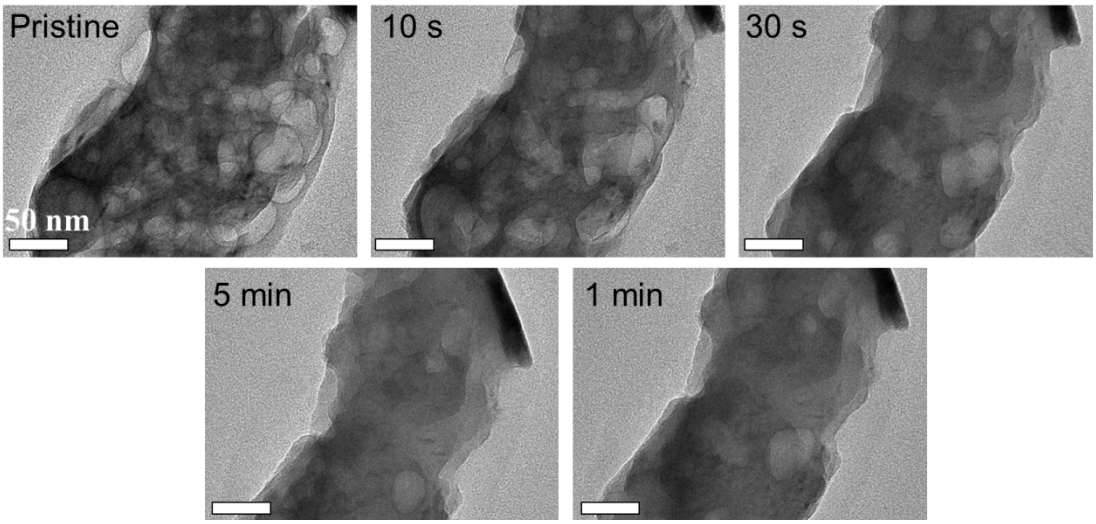

Supplementary Figure 6. TEM images of in-situ changes of the oBP nanosheets with the electron beam irradiation time, indicating the instability of porous structure under electron irradiation.

Supplementary Figure 6 shows the TEM images of the in-situ changes of oBP nanosheets with the long-time electron beam irradiation in vacuum. The porous structure in the oBP nanosheet is clear in the pristine image, and however, with the increase of the electron beam irradiation time, the pores gradually diffuse, coalesce and remove. After 5 min irradiation, most of the pores disappear, and the size of the oBP nanosheet decreases owing to water evaporation.

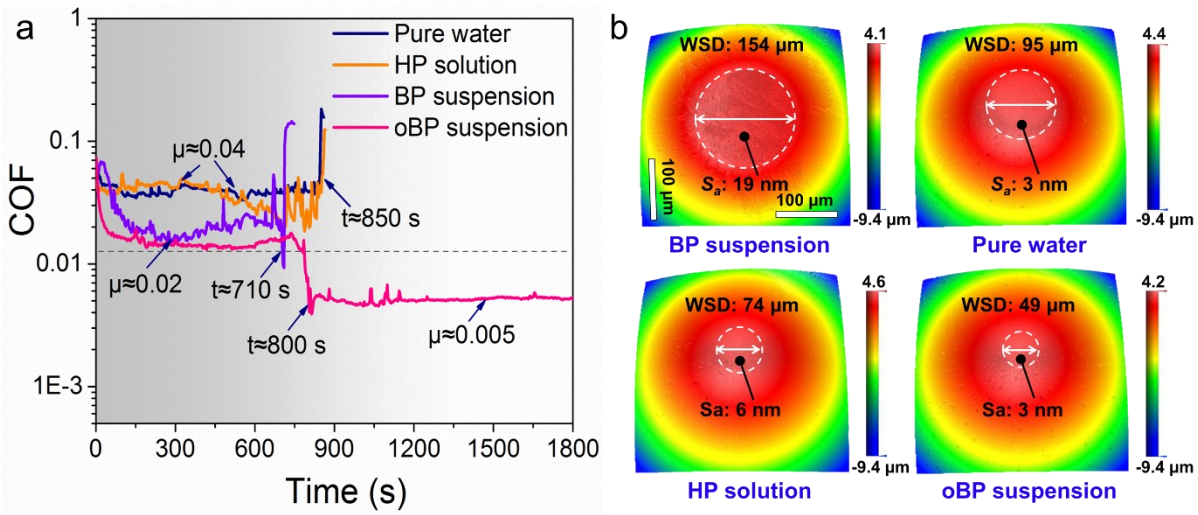

Supplementary Figure 7. (a) COFs versus time with the lubrication of pure water, the HP solution, the BP particles suspension and the oBP nanosheets suspension, showing the liquid superlubricity behavior of oBP nanosheets (2 N, 100 mm/s). **(b)** 3D topographic images showing the wear scars of the balls after testing with water, HP solution, BP suspension and oBP suspension.

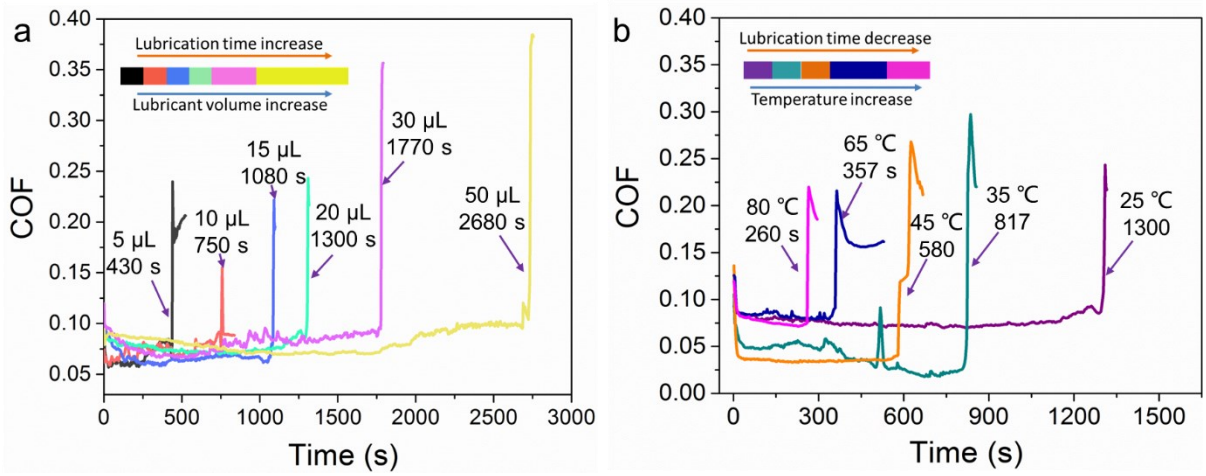

Supplementary Figure 8. COFs versus time with the lubrication of **(a)** different volumes water at 25 ˚C and **(b)** 20 μL water at different temperatures.

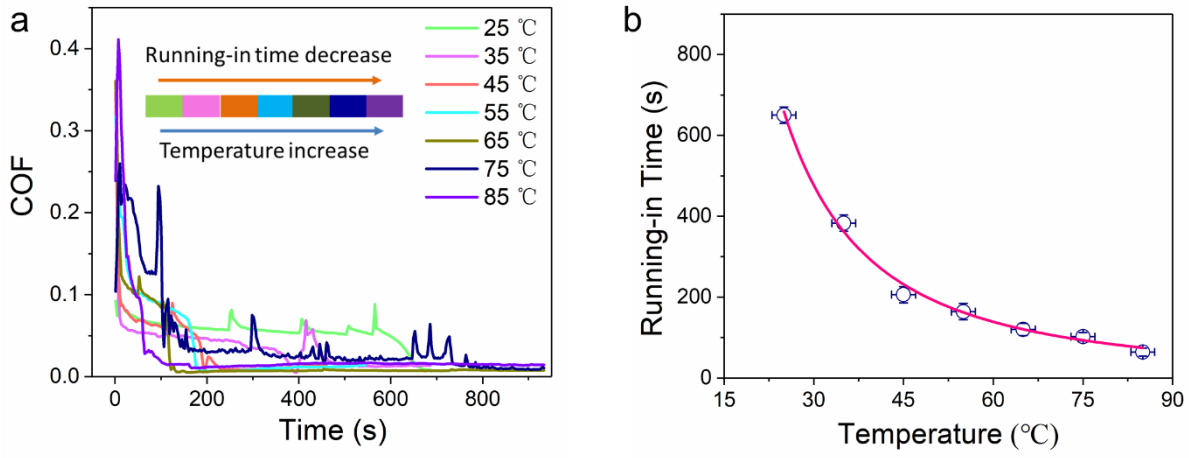

Supplementary Figure 9. (a) COFs versus time with the lubrication of oBP nanosheets suspensions at different temperatures. **(b)** The relation of the running-time with the test temperature and its fitting curve.

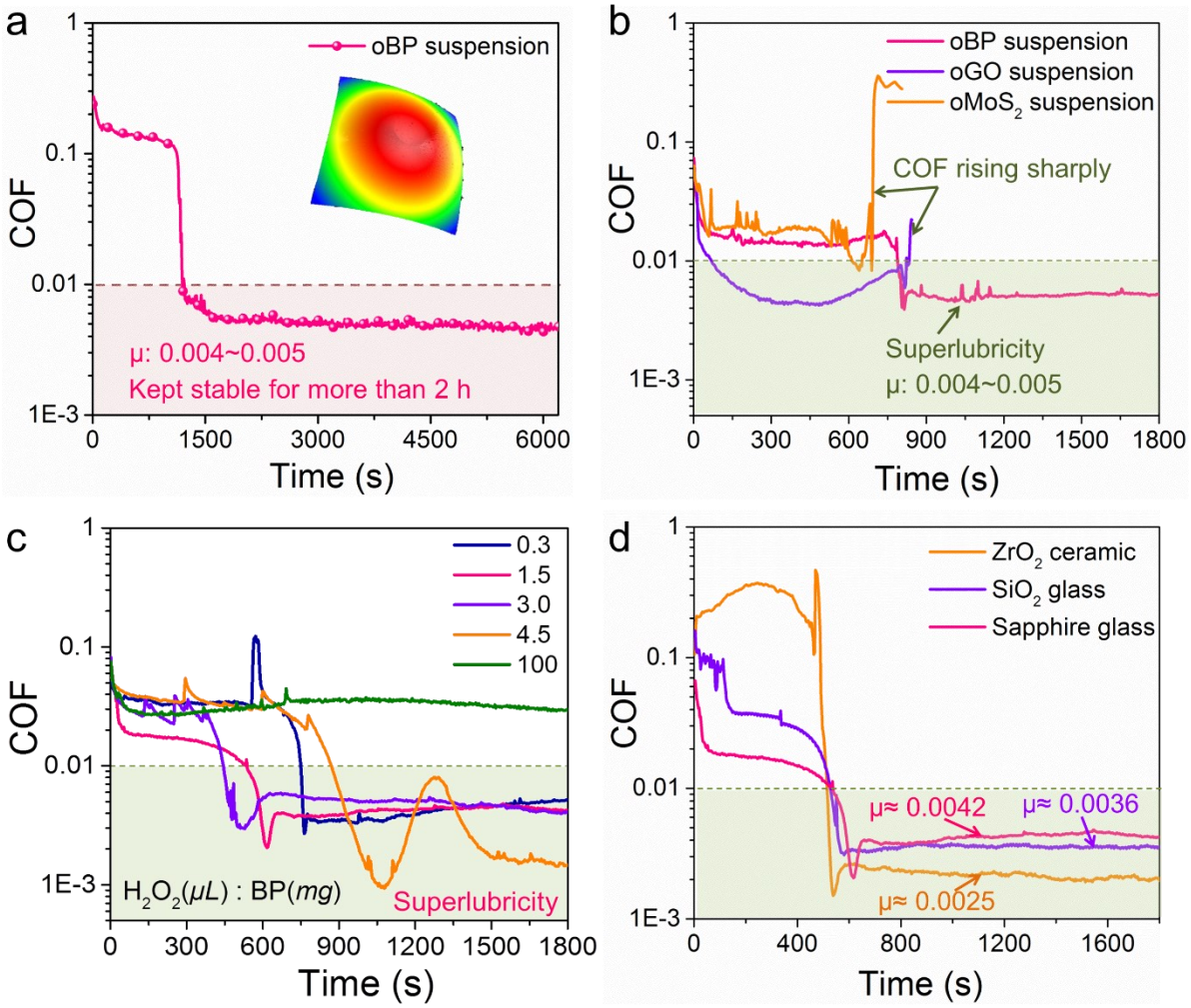

Supplementary Figure 10. (a) Long-time friction tests with the lubrication of 20 μL oBP nanosheets suspension (test condition: 3 N and 100 mm/s), showing that the superlubricity state can be kept stable for more than 2 h. **(b)** COFs versus time with the lubrication of 20 μL oBP, oGO, and $oMoS_2$ nanosheets suspensions (test condition: 2 N and 100 mm/s). **(c)** COFs versus time with the lubrication of 20 μL oBP nanosheets suspensions with different ratios of BP (*mg*) and HP (*μL*) (test condition: 2 N and 100 mm/s). **(d)** COFs versus time with the lubrication of 20 μL oBP nanosheets suspension with different substrate discs (test condition: 2 N and 100 mm/s).

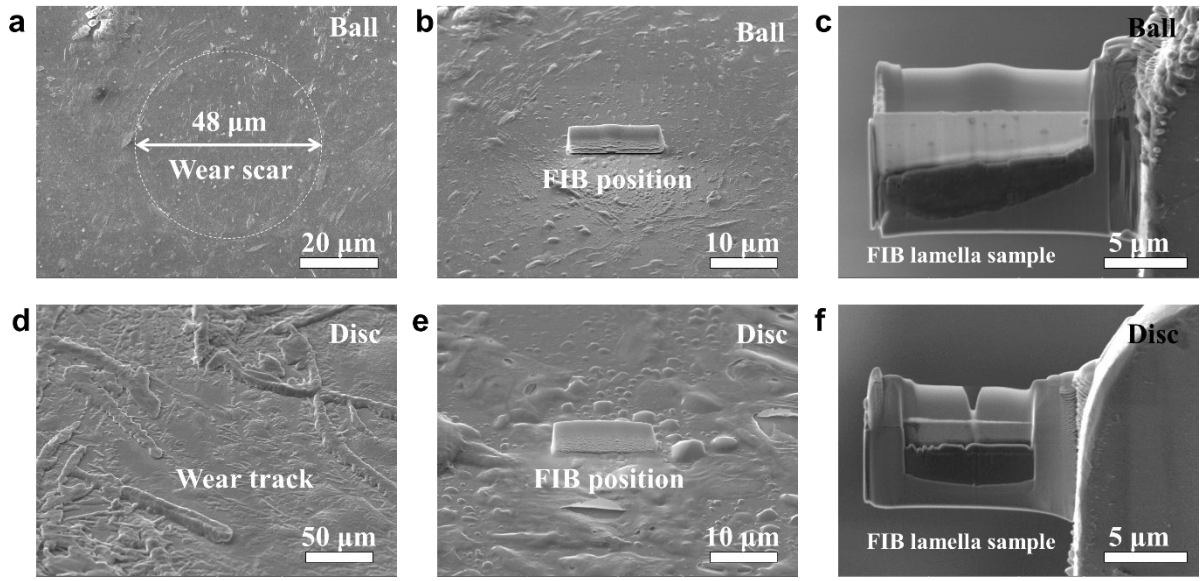

Supplementary Figure 11. SEM images on the wear scar of the Si_3N_4 ball **(a-c)** and the wear track of the sapphire disc **(d-f)** after the friction test with the oBP nanosheets suspension and drying under the vacuum condition (test condition: 2 N, 100 mm/s). **(b and e)** showing the FIB position on the wear surfaces and **(c and f)** showing the FIB lamella samples on the wear scar of the ball and the wear track of the disc. The friction pairs were dried under the vacuum condition without cleaning the wear surface.

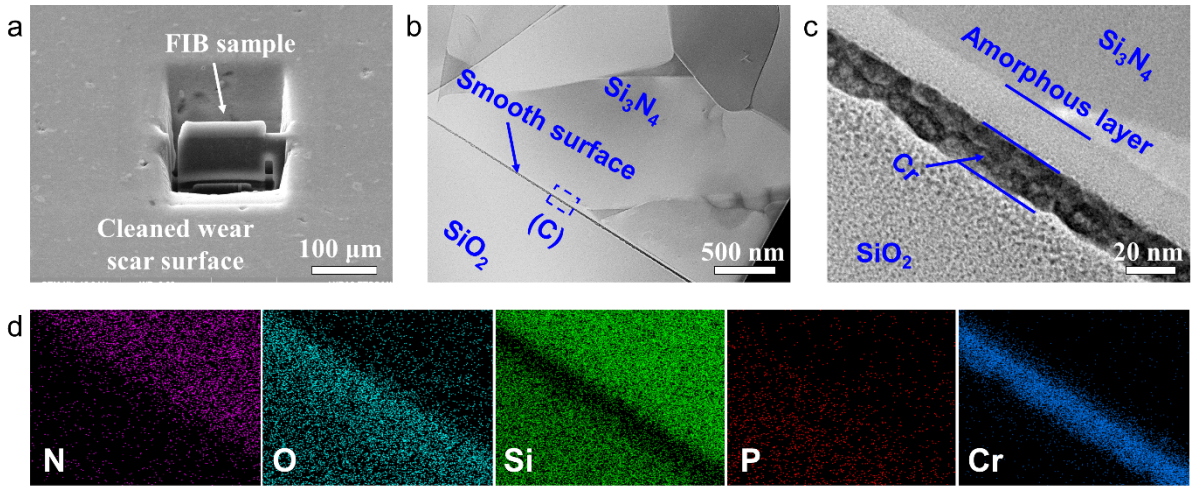

Supplementary Figure 12. (a) SEM image on the wear scar of the Si_3N_4 ball lubricated with the oBP suspension. The surface was cleaned by ethanol and water in sequence after the friction test. **(b and c)** TEM images showing the interfacial microstructures of the wear scar on the ball surface. **(d)** The corresponding EDS maps, indicating the distributions of P, O, Si, Cr, and N elements.

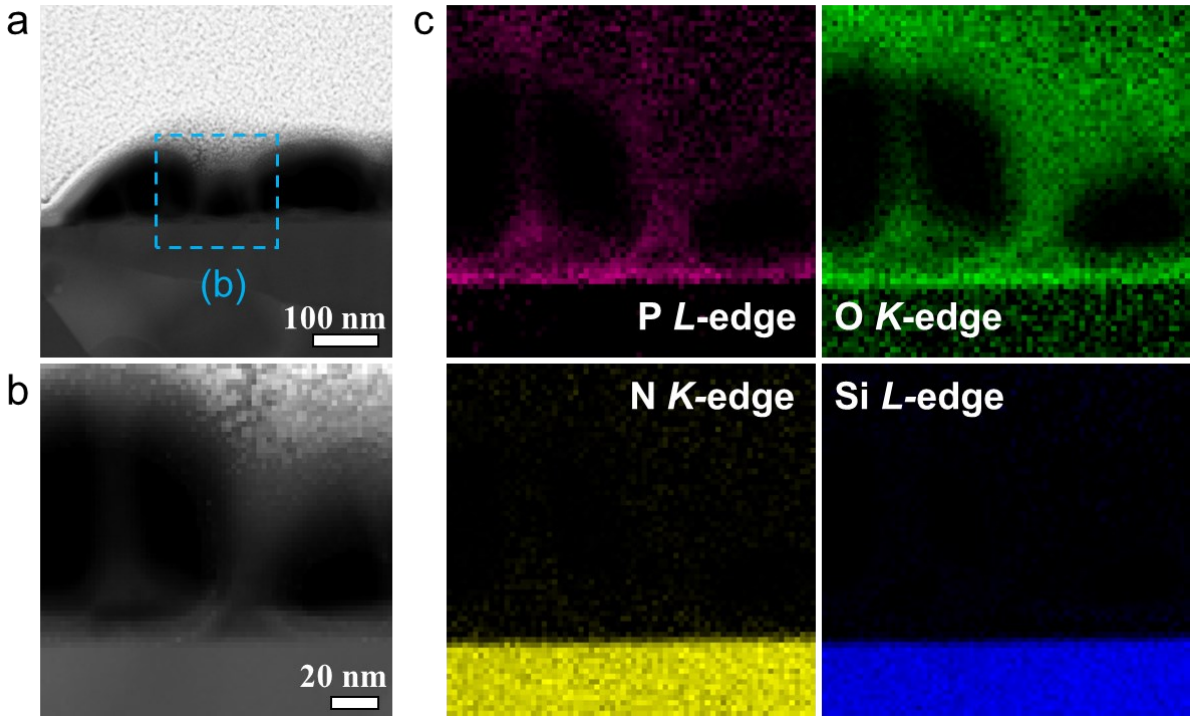

Supplementary Figure 13. (a) HAADF-STEM image showing the cross-sectional morphology of the wear scar surface lubricated with the oBP nanosheets suspension. **(b)** HAADF-STEM image as marked in (a), showing the EELS mapping zone. **(c)** EELS P-*L*, O-*K*, N-*K* and Si-*L* maps of the wear scar surface as shown in (b).

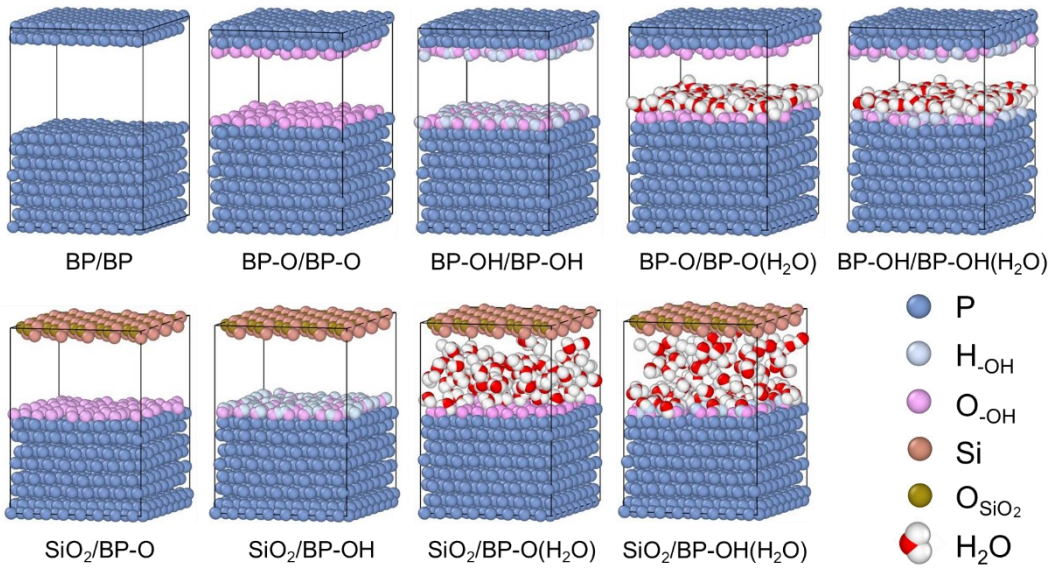

Supplementary Figure 14. The optimized simulated system models in this work.

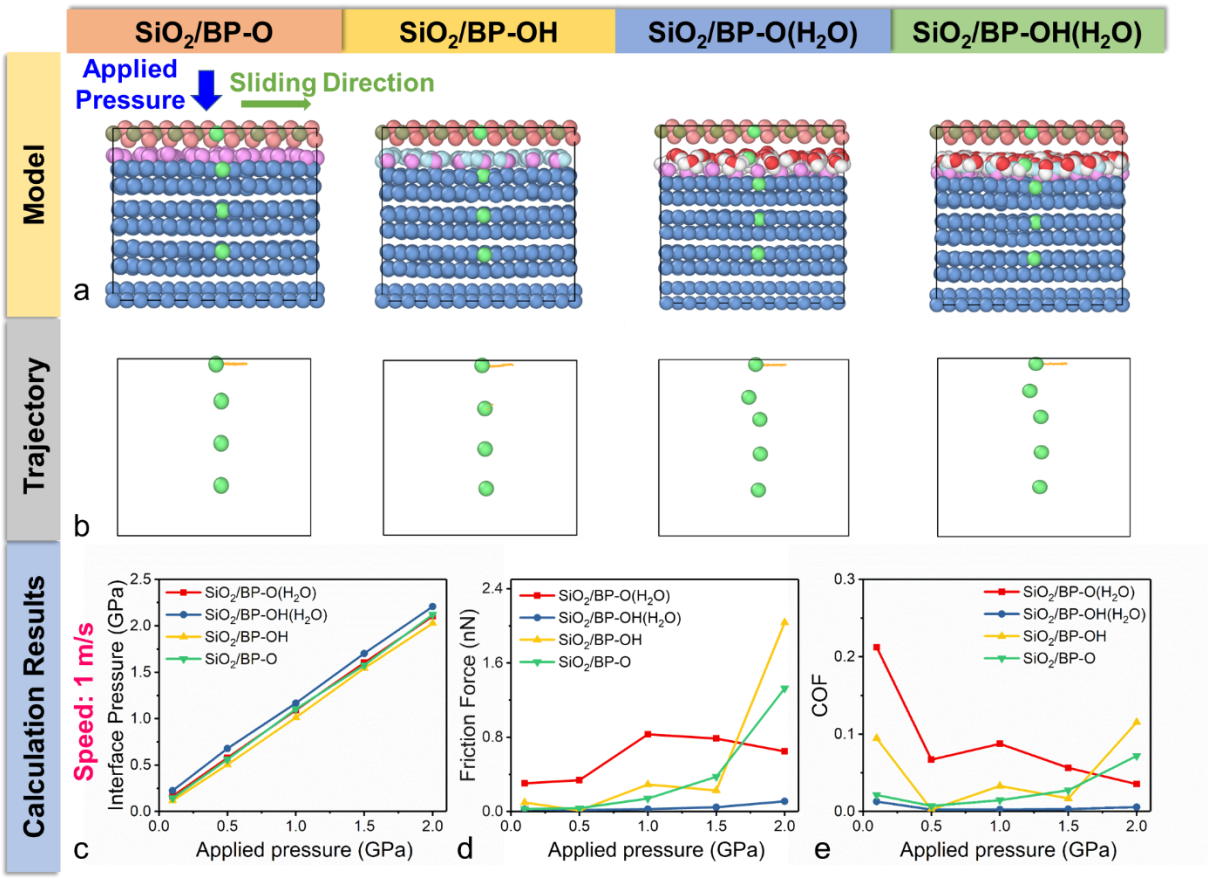

Supplementary Figure 15. Molecular dynamics (MD) simulation results for the SiO_2/BP-O and SiO_2/BP-OH friction interfaces with single-layer water molecules adsorbed on the oBP surface. **(a)** Models of the SiO_2/BP-OH and SiO_2/BP-O friction interfaces without the adsorption of water molecules and with the adsorption of single-layer water molecules. **(b)** Trajectories of the different layers in the model under the applied pressure of 1 GPa and the speed of 1 m/s, in which the green atoms are marked as the references. **(c-e)** Interface pressures, friction forces and COFs versus various applied pressures at the sliding speed of 1 m/s.

As shown in **Supplementary Figure 15 (a and b)**, the trajectories of the layers indicate that the sliding process mainly occurs between the loading layer (SiO_2) and the substrate layer (BP-O or BP-OH) at the SiO_2/BP-O and SiO_2/BP-OH friction interfaces with or without the adsorption of water molecules. Owing to the ultralow friction force between the SiO_2 layer and adsorbed water layer in the SiO_2/BP-OH(H_2O) system (**Supplementary Figure 15 d**), the extremely low COFs of around 0.003 at applied pressures of 0.5~2.0 GPa are obtained, being in agreement with the achievement of the superlubricity in the experiments.

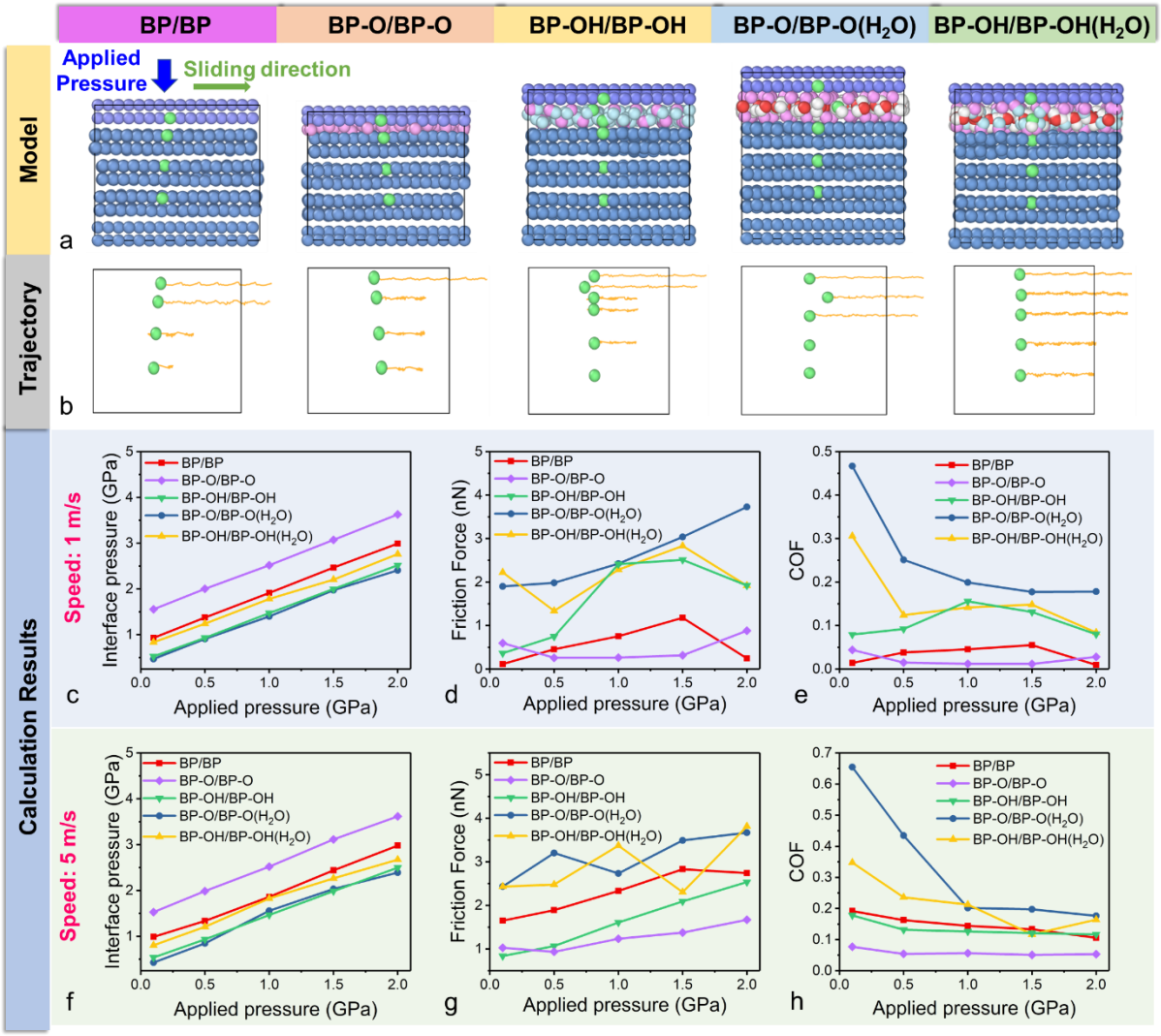

Supplementary Figure 16. MD simulation results for the BP/BP, BP-O/BP-O and BP-OH/BP-OH friction interfaces with or without single-layer water molecules. **(a)** Models of BP/BP, BP-O/BP-O and BP-OH/BP-OH friction interfaces with or without single-layer water. **(b)** Trajectory of the different layers in the model under the applied pressure of 1 GPa and the speed of 1 m/s, in which the green atoms are marked as the references. Interface pressures, friction forces and COFs versus various applied pressures at the speeds of **(c-e)**1 m/s and **(f-g)** 5 m/s.

Supplementary Figure 16 shows the MD simulation results for the BP/BP, BP-O/BP-O and BP-OH/BP-OH friction interfaces with or without single-layer water molecules. The trajectories of the layers indicate that the sliding processes at the friction interfaces in the BP-O/BP-O and BP-OH/BP-OH systems mainly occur between the substrate layers with the adsorption of single-layer water molecules (**Supplementary Figure 16 (a and b)**). The strong hydrogen bonds make the single-layer water molecules glue onto the upper and lower layers at the interfaces. Therefore, the COFs at the

friction interfaces in the BP-O/BP-O and BP-OH/BP-OH systems with single-layer water molecules are even higher than those without water molecules.

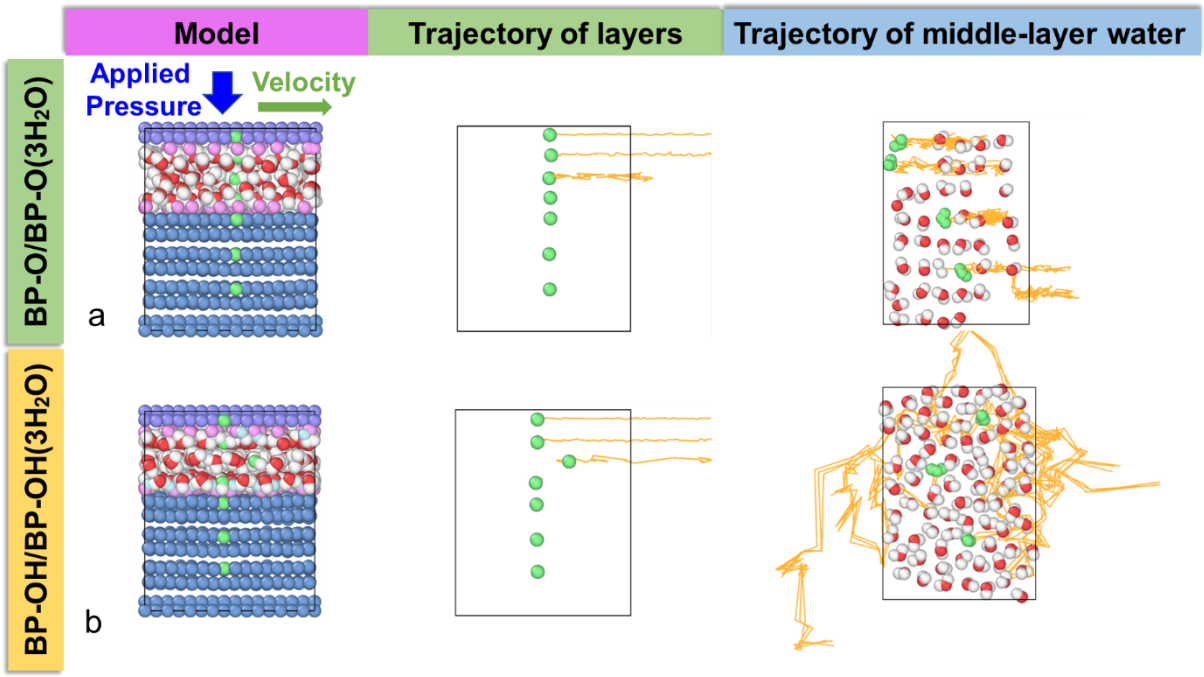

Supplementary Figure 17. MD simulation models and the trajectories of the layers at the friction interfaces in the BP-O/BP-O **(a)** and the BP-OH/BP-OH systems **(b)** with three-layers water molecules.

However, in consideration of the strong hydrogen bonding, more layers of water molecules may be present at the friction interfaces when more water molecules are involved. The friction behavior at the interfaces in the BP-O/BP-O and BP-OH/BP-OH interfaces with three-layer water molecules were also investigated, and the results are shown in **Supplementary Figure 17** and **18**. When three-layer water molecules are involved at the interfaces, the COFs are much lower than those without the adsorption of water molecules. A superlubricity state with a COF of 0.0017 is even achieved at the friction interface in the BP-OH/BP-OH system. The trajectories suggest that the middle one in the three-layer water molecules is prone to slipping, resulting in the superlow COF at the BP-OH/BP-OH interface with three-layer water molecules (**Supplementary Figure 17** and **18**).

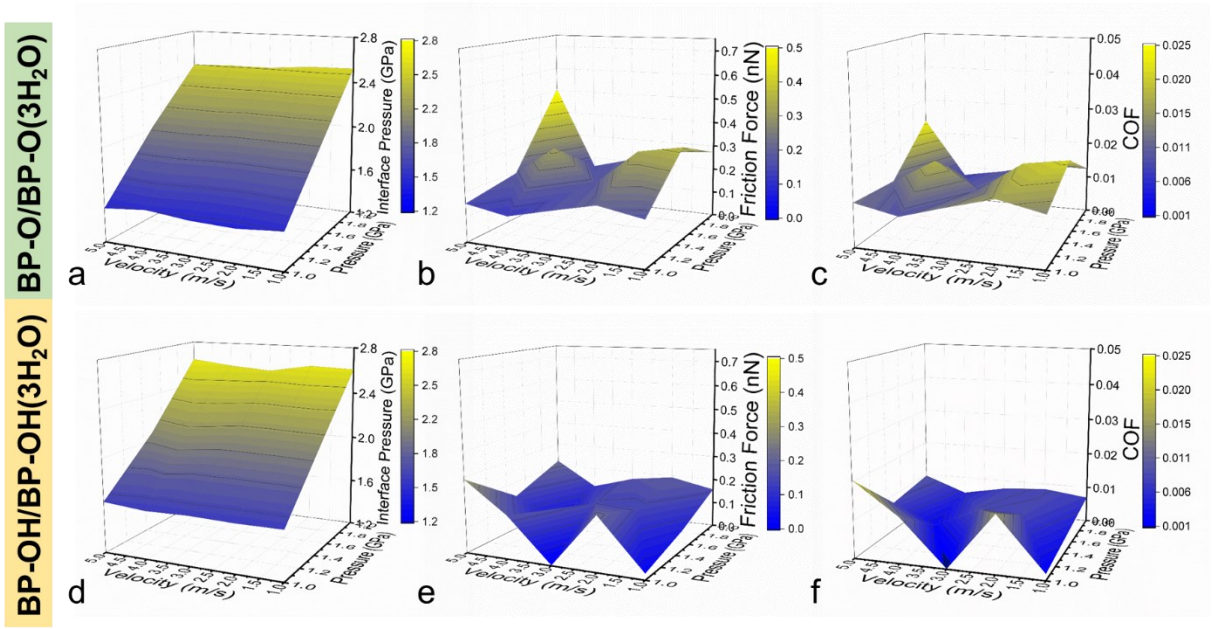

Supplementary Figure 18. Interface pressures, friction forces and COFs of the MD simulation results versus various applied pressures (1~2 GPa) and sliding speeds (1~5 m/s) for the BP-O/BP-O **(a-c)** and BP-OH/BP-OH **(d-f)** friction interfaces with three-layers water molecules.

2. Supplementary Tables

Supplementary Table 1. Wear scar diameters (WSD), contact pressures (CP) and COFs with the lubrication of oBP nanosheets suspensions under various test conditions during the superlubricity state.

Test conditions		WSD (μm)	CP (MPa)	COF
Various loads with 100 mm/s velocity. Unit: N	1	40.15 ± 2.12	794 ± 84	0.0059 ± 0.0022
	2	49.41 ± 1.26	1044 ± 53	0.0033 ± 0.0023
	3	70.05 ± 8.10	802 ± 203	0.0051 ± 0.0023
	4	84.96 ± 6.09	713 ± 106	0.0048 ± 0.0011
Various velocities with 2 N load Unit: mm/s	50	61.13 ± 0.61	682 ± 13	0.0053 ± 0.0011
	100	49.41 ± 1.26	1044 ± 53	0.0033 ± 0.0023
	150	49.30 ± 0.85	1048 ± 36	0.0049 ± 0.0005
	200	47.14 ± 1.36	1148 ± 68	0.0065 ± 0.0006
	250	46.22 ± 1.29	1193 ± 65	0.0068 ± 0.0011
Various ratios of HP to BP with 2 N load and 100 mm/s velocity	0.3	63.02 ± 0.86	641 ± 17	0.0043 ± 0.0009
	1.5	49.41 ± 1.26	1044 ± 53	0.0033 ± 0.0023
	3	52.77 ± 2.41	918 ± 83	0.0046 ± 0.0011
	4.5	57.80 ± 1.40	763 ± 37	0.0059 ± 0.0021
	100	100.87 ± 1.42	250 ± 7	0.032 ± 0.0026

Supplementary Table 2. The fractions of the elements in each layer as shown in Fig. 4 d. The points are marked in Fig. 4 c.

EDS Points	P (at.%)	O (at.%)	Si (at.%)	Cr (at.%)	N (at.%)
1	1.93	46.98	25.33	25.76	0
2	8.84	24.73	4.73	59.65	2.05
3	0.88	12.90	41.33	1.50	43.39
4	0.05	3.18	47.23	0.05	49.49

Supplementary Table 3. Universal force field (UFF) potential parameters of the bonding coefficients and the angle coefficients; and the Lennard–Jones (L-J) potential parameters of σ and ε for the studied models.

UFF potential parameters of the bond coefficients		k_{ij} (eV)	r (Å)
	P_{BP} - $O_{oxide\text{-}BP}$	67.650	1.8680
	$O_{hydroxyl}$ - $H_{hydroxyl}$	23.445	0.9572
	O_{H2O} – H_{H2O}	23.445	1.0000
UFF potential parameters of the angel coefficients		k_{ijk} (eV)	θ (Å)
	P_{BP} - $O_{hydroxyl}$ - $H_{hydroxyl}$	3.917	110.70
	H_{H2O} - O_{H2O} – H_{H2O}	2.168	109.47
	P_{BP} – P_{BP}- $O_{oxide\text{-}BP}$	3.486	158.75
L-J potential parameters σ and ε		σ (Å)	Ɛ (eV)
	P_{BP}-O_{H2O}	3.7418	0.008673
	O_{H2O}-$O_{hydroxyl}$	2.6000	0.000650
	O_{H2O}-$O_{oxide\text{-}BP}$	2.6000	0.000650
	Si_{SiO2}-H_{H2O}	3.5910	0.005800
	O_{SiO2}-H_{H2O}	2.6000	0.000650
	Si_{SiO2}-O_{H2O}	3.4900	0.010824
	O_{SiO2}-O_{H2O}	3.1360	0.004180
L-J potential parameters σ and ε for hydrogen bonds		σ (Å)	Ɛ (eV)
	$O_{hydroxyl}$-H_{H2O}	1.4650	0.35938
	$H_{hydroxyl}$-H_{H2O}	1.4650	0.35938
	$O_{oxide\text{-}BP}$-H_{H2O}	2.12450	0.2568